Pure appl. geophys. 165 (2008) 903–922
0033–4553/08/050903–20
DOI 10.1007/s00024-008-0338-4

Pure and Applied Geophysics

Rayleigh-Wave Dispersive Energy Imaging Using a High-Resolution Linear Radon Transform

YINHE LUO,[1] JIANGHAI XIA,[2] RICHARD D. MILLER,[2] YIXIAN XU,[3] JIANGPING LIU,[1] and QINGSHENG LIU[1]

Abstract—Multichannel Analysis of Surface Waves (MASW) analysis is an efficient tool to obtain the vertical shear-wave profile. One of the key steps in the MASW method is to generate an image of dispersive energy in the frequency-velocity domain, so dispersion curves can be determined by picking peaks of dispersion energy. In this paper, we propose to image Rayleigh-wave dispersive energy by high-resolution linear Radon transform (LRT). The shot gather is first transformed along the time direction to the frequency domain and then the Rayleigh-wave dispersive energy can be imaged by high-resolution LRT using a weighted preconditioned conjugate gradient algorithm. Synthetic data with a set of linear events are presented to show the process of generating dispersive energy. Results of synthetic and real-world examples demonstrate that, compared with the slant stacking algorithm, high-resolution LRT can improve the resolution of images of dispersion energy by more than 50%.

Key words: MASW, Rayleigh-wave, dispersive energy, high-resolution, linear Radon transform, conjugate gradient.

1. Introduction

Multichannel Analysis of Surface Waves (MASW) analysis is an efficient tool to obtain the vertical shear (S)-wave velocity profile (e.g., MCMECHAN and YEDLIN, 1981; SONG *et al.*, 1989; XIA *et al.*, 1999, 2002a, b, 2006a; PARK *et al.*, 1999; CALDERÓN-MACÍAS and LUKE, 2007; LUO *et al.*, 2007). Large amplitudes of surface waves allow accurate reconstruction of shallow structures in a noisy environment via inversion of observed dispersion curves (XIA *et al.*, 2004). MASW techniques, therefore, have been widely applied in Near-surface applications: near-surface attenuation parameters (XIA *et al.*, 2002c), bedrock mapping (XIA *et al.*, 1998; MILLER *et al.*, 1999), cavern detection (XIA *et al.*, 2004, 2007a) joint inversion of P-wave velocities and surface wave phase velocities (DAL MORO and PIPAN,

[1] Institute of Geophysics and Geomatics, China University of Geosciences, Wuhan, Hubei 430074, China E-mail: yluo@kgs.ku.edu; luoyinhe@cug.edu.cn

[2] Kansas Geological Survey, The University of Kansas, 1930 Constant Avenue, Lawrence, Kansas 66047-3724, USA.

[3] State Key Laboratory of Geological Processes and Mineral Resources, Institute of Geophysics and Geomatics, China University of Geosciences, Wuhan, Hubei 430074, China.

2007; IVANOV *et al.*, 2006a), and other nondestructive detection projects (TIAN *et al.*, 2003a,b; LAI *et al.*, 2002; YILMAZ and ESER, 2002; IVANOV *et al.*, 2006b).

The MASW method utilizes a multichannel recording system to estimate near-surface S-wave velocity from high-frequency Rayleigh waves. This technique consists of (1) acquisition of wide-band, high-frequency ground roll using a multichannel recording system (e.g., SONG *et al.*, 1989); (2) creation of efficient and accurate algorithms organized in a straightforward data-processing sequence designed to extract and analyze 1D Rayleigh-wave dispersion curves (e.g., YILMAZ, 1987; MCMECHAN and YEDLIN, 1981; PARK *et al.*, 1998; XIA *et al.*, 2007b); (3) development of stable and efficient inversion algorithms to obtain S-wave velocity profiles (e.g., XIA *et al.*, 1999), and (4) construction of the 2D S-wave velocity field (XIA *et al.*, 1998; MILLER *et al.*, 1999).

Generating a reliable image of dispersion energy in the frequency-velocity (*f-v*) domain is a key step in the MASW method. Four algorithms are available in calculating image of high-frequency dispersion energy: The F-K transformation (e.g., YILMAZ, 1987), the tau-p transform (MCMECHAN and YEDLIN, 1981), and the phase shift (PARK *et al.*, 1998). DAL MORO *et al.* (2003) evaluated the effectiveness of three computational schemes for phase-velocity computation based on F-K spectrum, tau-p transform, and phase shift. They concluded that phase-shift approach is insensitive to data processing and performs very well even when a limited number of traces are considered. XIA *et al.* (2007b) developed an algorithm that can be applied to data acquired with receivers in an arbitrary acquisition geometry, which consists of two steps: stretching data into pseudo-vibroseis data or frequency-swept data, and slant stacking frequency-swept data. This method presents a solution to 3D S-wave velocity mapping.

The efficiency of algorithms for phase-velocity determination can be evaluated in terms of resolution, noise content, and computation times (DAL MORO *et al.*, 2003). Noise content can be solved by using the standard CMP (common midpoint) roll-along acquisition (MAYNE, 1962) system to record surface-wave data (XIA *et al.*, 1998, 2004; MILLER *et al.*, 1999), and computation times can also be satisfied for fast developed computer techniques. Nevertheless, improving the resolution of dispersion image in the frequency–velocity (*f-v*) domain is a meaningful and challenging task in the MASW method. High-resolution image of dispersive energy can help us correctly pick dispersion curves and separate the fundamental mode from higher modes of surface waves. Modeling results (PARK *et al.*, 1998) show that resolution of the dispersion image in the *f-v* domain increases as the geophone spread increases. Generally, resolution of the dispersion image could vary with algorithms that were used to generate dispersion image in the *f-v* domain; four algorithms discussed below image the dispersive energy of surface waves with the same level of resolution.

The four algorithms mentioned previously are kinds of standard discretized linear Radon transform (LRT). Because standard LRT suffers from typical problems of loss of resolution and aliasing that arise as consequence of incomplete information, including limited aperture and discretization (TRAD *et al.*, 2003), achieving a high resolution dispersion image with a standard LRT is difficult. An appealing alternative solution to

efficiently image dispersive energy can be obtained by high-resolution LRT (SACCHI and ULRYCH, 1995; SCHONEWILLE and DUIJNDAM, 2001; TRAD *et al*., 2002, 2003; ETHAN and MATTHIAS, 2006). Because high-resolution LRT attenuates aliasing and improves resolution to some degree by use of sparseness inversion technique, it can image dispersion energy with higher resolution.

In this paper, we propose to image Rayleigh-wave dispersive energy by high-resolution LRT. We first introduce the standard and high-resolution LRT and present synthetic data to show the process of generating images of dispersive energy. Then we generate images of Rayleigh-wave dispersion energy of synthetic and real-world data to demonstrate the feasibility of using high-resolution LRT to image higher-resolution dispersion energy.

2. *Linear Radon Transform*

In this section, we first introduce the standard and high-resolution LRT. Then we present synthetic data to show the process of generating dispersive energy.

2.1. *Standard LRT*

The linear Radon transform (LRT) is a plane-wave decomposition achieved by applying a linear moveout to data and summing over amplitudes (YILMAZ, 1987), which maps the Radon domain m(p, τ) into the data space $d(x,t)$ (recorded data) as follows:

$$d(x,t) = \sum_{p=p_{\min}}^{p_{\max}} m(p, \tau = t - px) \tag{1}$$

and the adjoint transformation

$$m(p,\tau) = \sum_{x=x_{\min}}^{x_{\max}} d(x, t = \tau + px), \tag{2}$$

where t is the time, τ is the zero offset intercept time, p the slowness ($p_{\min}$ and $p_{\max}$ being the range of slowness values investigated), and x the offset between source and receiver ($x_{\min}$ and $x_{\max}$ being the offset range). The LRT has various applications (TURNER, 1990; DUNNE and BERESFORD, 1995; ZHOU and GREENHALGH, 1994; LUIGIA and TATIANA, 2004; MAELAND, 2004; WILSON and GUITTON, 2007).

After a temporal Fourier transformation, the LRT can be calculated for each temporal frequency component f :

$$d(x,f) = \sum_{p=p_{\min}}^{p_{\max}} m(p,f) e^{i2\pi fpx} \tag{3}$$

and

$$m(p,f) = \sum_{x=x_{\min}}^{x_{\max}} d(x,f)e^{-i2\pi fpx}. \tag{4}$$

Formula (3) can be written in matrix form as follows:

$$\mathbf{d} = \mathbf{L}\mathbf{m}, \tag{5}$$

where $\mathbf{L} = e^{i2\pi fpx}$ is the forward LRT operator, and $\mathbf{d}$ and $\mathbf{m}$ represent the shot gather and Radon panel after lexicographic arrangement, respectively.

Similarly, formula (4) can be rearranged, and represented in a matrix form as

$$\mathbf{m}_{\text{adj}} = \mathbf{L}^T\mathbf{d}, \tag{6}$$

where $\mathbf{m}_{\text{adj}}$ denotes a low-resolution Radon panel using the transpose or adjoint operator $\mathbf{L}^T$. It is clear that because $\mathbf{L}$ is not a unitary operator, $\mathbf{L}^T$ does not define the inverse operator. The F-K transformation (e.g., YILMAZ, 1987), the tau-p transform (MCMECHAN and YEDLIN, 1981), the phase shift (PARK *et al.*, 1998), and the slant stacking (XIA *et al.*, 2007b) commonly used in high-frequency surface-wave analysis are fundamentally kinds of standard discretized LRT. For example, the slant-stacking method (XIA *et al.*, 2007b) firstly stretches recorded data into pseudo-vibroseis data or frequency-swept data (CORUH, 1985), then performs LRT to frequency-swept data by formula (2), and finally transforms the Radon panel from the time-velocity domain to the *f-v* domain to achieve dispersive energy. Because standard LRT suffers from the typical problems of loss of resolution and aliasing that arise as consequence of incomplete information, including limited aperture and discretization (TRAD *et al.*, 2003), it is hard to achieve high-resolution images of dispersion energy.

2.2. The Least-Square LRT

THORSON and CLAERBOUT (1985) proposed inverting equation (1) rather than using the low-resolution LRT $\mathbf{L}^T$. For that purpose, they proposed a stochastic inversion technique that is able to retrieve a sparse Radon panel. A similar technique has been developed by SACCHI and ULRYCH (1995) to invert time-invariant Radon operators in the frequency domain.

Traditionally, three possibilities exist for the forward problem of formula (5); namely, the system can be over-, under-, or mixed-determined. In practice, however, the data parameters may be linearly dependent, suggesting a rank-deficient, slightly underdetermined or mixed-determined problem. Hence, we only discuss mixed-determined solutions of LRT.

Casting LRT as an inversion for a model that generates the data under the action of operator $\mathbf{L}$, we can find the vast arsenal of tools available from inverse theory (MENKE, 1984; TARANTOLA, 1987). The idea is to find $\mathbf{m}$ such that the following objective function is minimized (YILMAZ and TANER, 1994):

$$J = \|\mathbf{d} - \mathbf{Lm}\|^2. \tag{7}$$

The solution to this problem is the least-square solution:

$$\mathbf{m} = (\mathbf{L}^T\mathbf{L})^{-1}\mathbf{L}^T\mathbf{d}. \tag{8}$$

In general, the inverse needs to be stabilized using a damping parameter λ,

$$\mathbf{m} = (\mathbf{L}^T\mathbf{L} + \lambda\mathbf{I})^{-1}\mathbf{L}^T\mathbf{d}. \tag{9}$$

Commonly, the least-square transform can give better reconstruction and better resolution in the Radon domain that allow better signal and noise separation (SCHONEWILLE and DUIJNDAM, 2001). However, a harmful by-product is an increase in the amplitude of aliased events in the Radon domain. These amplified aliases degrade signal periodicity in the Radon domain (MARFURT and SCHNEIDER, 1996) and will cause consequence problems for imaging dispersive energy such as body-wave suppressing, multimode separation, and so on.

2.3. High Resolution LRT

To find the model **m** that best fits the data and minimize the number of the model space parameters necessary to represent the data in the Radon domain, sparsity constraint should be considered. As explained in CLAERBOUT (1992), many inversion schemes can be implemented by conjugate gradient (CG) techniques just finding the forward and adjoint operators. We use a weighted preconditioned CG to perform high-resolution LRT (e.g., SACCHI and ULRYCH, 1995). The weighting allows a softening of the data constraint for bad or noised data. The preconditioning allows a sparse solution, which can be achieved by applying a right preconditioning and equation (5) becomes (TRAD *et al.*, 2002):

$$\mathbf{d} = \mathbf{L}\mathbf{W}_m^{-1}\mathbf{W}_m\mathbf{m}. \tag{10}$$

The idea is to find **m** so that the following objective function is minimized (TRAD *et al.*, 2002):

$$J = \left\|\mathbf{W}_d(\mathbf{d} - \mathbf{L}\mathbf{W}_m^{-1}\mathbf{W}_m\mathbf{m})\right\|^2 + \lambda\|\mathbf{W}_m\mathbf{m}\|^2. \tag{11}$$

Thus, the model can be founded by solving the following equation (TRAD *et al.*, 2003):

$$(\mathbf{W}_m^{-T}\mathbf{L}^T\mathbf{W}_d^T\mathbf{W}_d\mathbf{L}\mathbf{W}_m^{-1} + \lambda\mathrm{I})\mathbf{W}_m\mathbf{m} = \mathbf{W}_m^{-T}\mathbf{L}^T\mathbf{W}_d^T\mathbf{W}_d\mathbf{d}. \tag{12}$$

where **I** denotes the identity matrix; $\mathbf{W}_d$ is a matrix of data weights, often a diagonal matrix determined by the standard deviation of residual **r** calculated by $\mathbf{r} = \mathbf{L}\mathbf{W}_m^{-1}\ \mathbf{W}_m\mathbf{m}\text{-}\mathbf{d}$; $\mathbf{W}_m$ is a matrix of model weights that plays an extremely important role in the design of high-resolution Radon operators, for example, resolution and smoothness (TRAD *et al.,*

2002, 2003) W_m^{-T} is the transpose matrix of W_m^{-1}; and the parameter λ controls the trade-off between the data misfit and model constraints.

The effect of right preconditioning is to set the model weights as part of the modeling rather than as a penalizing factor in the cost function, and the weighting factors $\mathbf{W}_m$ we apply act as a kind of preconditioner whose function is not to decrease the condition number of the matrix but rather to focus the "best" subspace of the solution space, which also is called a sparse solution. Formula (12) can be solved very efficiently by CG algorithm, and details of the strategy can be found in many literatures (TARANTOLA, 1987; MENKE, 1984; SACCHI and PORSANI, 1999; TRAD *et al.*, 2002; 2003; JI, 2006). The weighting and the preconditioning matrices $\mathbf{W}_d$ and $\mathbf{W}_m$ at the i-th iteration of the CG algorithm are determined by using diagonal matrices: $\mathrm{diag}(\mathbf{W}_\mathrm{d})_\mathrm{i} = |\mathrm{r_i}|^{-1/2}$ and $\mathrm{diag}(\mathbf{W}_m)_i = |m_i|^{1/2}$, respectively, where m_i is the Radon model at i-th iteration of the CG algorithm, r_i is the standard deviation of residual $\mathbf{r}$ (HERRMANN *et al.*, 2000; TRAD *et al.*, 2002, 2003; JI, 2006).

2.4. Process of Generating Dispersive Energy

Synthetic data that consist of a set of linear events with different velocities (80, 100, 125 150,170 m/s) were used to illustrate the process of imaging dispersive energy by the LRT. Figure 1a shows the synthetic data containing 48 traces with 1 m interval and null minimum offset. For comparison, we perform the transform by standard LRT and high-resolution LRT.

First, we transform the data according to formula (5). We transform the shot gather along the time direction to the frequency domain and set the slowness p range from 0 s/m to 0.02 s/m with 0.0001 s/m interval (201 slowness points) and the offset x range from 0 m to 47 m with 1 m interval (48 traces). One should notice that the choice of sampling of p values requires avoiding aliasing for correctly reconstructing the original image; we choose p range and interval properly according to the widely used rule proposed by TURNER (1990). Now we get $\mathbf{d}$ and $\mathbf{L}$, and Radon panel $\mathbf{m}$ is the aim of the next stage.

Then the LRT is done for each frequency slice. Standard LRT uses the adjoint operator $\mathbf{L}^T$ to carry out transform (formula (6)) and high-resolution LRT uses a weighted preconditioned CG algorithm to perform transform (formula (12)).

Finally, the data are transformed back along the time coordinate, and we obtain the Radon panel in the τ-p domain.

Linear interpolation is used to transform the Radon panel from the slowness-frequency domain to the f-v domain. Figures 1b and 1d show the Radon panel in the f-v domain calculated by standard LRT and high-resolution LRT. Figures 1c and 1e show the Radon panel in the τ-p domain, correspondingly. We notice that (1) near-offset data generate tails with constant traveltimes, while the far offsets generate tails cutting diagonally across the Radon domain as observed in Figure 1c, which occurs because standard LRT hardly deals with aliasing and artifact caused by spatial truncation (the limited size of spatial aperture of the shot gather) (WANG, 2003; ETHAN and MATTHIAS, 2006). When high-resolution LRT

is used, however, the events are tightly located in the Radon domain without noticeable tails as shown in Figure 1e. This phenomenon correspondingly occurs in Figures 1b and 1d; (2) high-resolution LRT uses a weighted preconditioned CG algorithm to perform transform and effectively deal with aliasing; the almost perfect result is sparse events in Figure 1e, while the result has considerably lower resolution by standard LRT, and (3) Figure 1d shows much higher resolution than Figure 1b. Forbriger (2003) provided an analytical result to assess resolution of the dispersion image as $R = 1/fC$ in the frequency-slowness domain, where R is the half-width between the neighboring minima of dispersion energy, f is the frequency, and C is the geophone spread. We realize that its counterpart in the f–v domain will contain phase velocity terms in the right side of the equation. To simplify our discussion, we directly use the length (L) between the half-value of dispersion energy at a given frequency to evaluate the resolution of dispersion energy imaged by an algorithm (Xia *et al*., 2006). If length L_A of dispersive energy at a certain frequency generated by algorithm A is twice as long as length L_B of dispersive energy at the same frequency which is generated by algorithm B, we deem that the resolution of dispersive energy which is generated by algorithm B increases 100%. To estimate resolution of the dispersion image, we use a double-end line at frequency 10 Hz at the center event between the half value of dispersion energy in Figure 1b and set the same length in Figure 1d. One can see that the double-end line almost spans twice us long than the half value, and the resolution increases more than 200% by using high-resolution LRT.

In Rayleigh-wave dispersive energy imaging, the first two steps are necessary and we perform RT in the frequency domain for dispersive energy imaging of surface waves because operators in the frequency domain have several important advantages over their counterparts in the time domain. First, if the computation is done properly inside the bandwidth of the signal, the waveforms are well preserved (Ethan and Matthias, 2006). Second, the action of the forward and adjoint operators can be computed by means of circular convolution in the frequency domain (Schonewille and Duijndam, 2001). Finally, time-variant RT produces the sparsest results both in τ and p directions, while in the frequency domain RT achieves the sparsest results both in f and p directions (Trad *et al*., 2002, 2003) which is a critical advantage in performing surface-wave multimode separation.

3. A Synthetic Example

A synthetic shot gather (the vertical component, Fig. 2a) due to a two-layer model was computed using a finite-difference method (Xu *et al*., 2007; Xia *et al*., 2007b). The model consists of the surface layer Vp = 800 m/s, Vs = 200 m/s, $\rho = 2000$ kg/m^3, and thickness h = 10 m, and the half-space Vp = 1200 m/s, Vs = 400 m/s, and $\rho = 2000$ kg/m^3. Dispersive energy of Rayleigh waves was clearly modeled in a synthetic shot gather with 60 channels (Fig. 2a). The nearest offset of the shot gather is

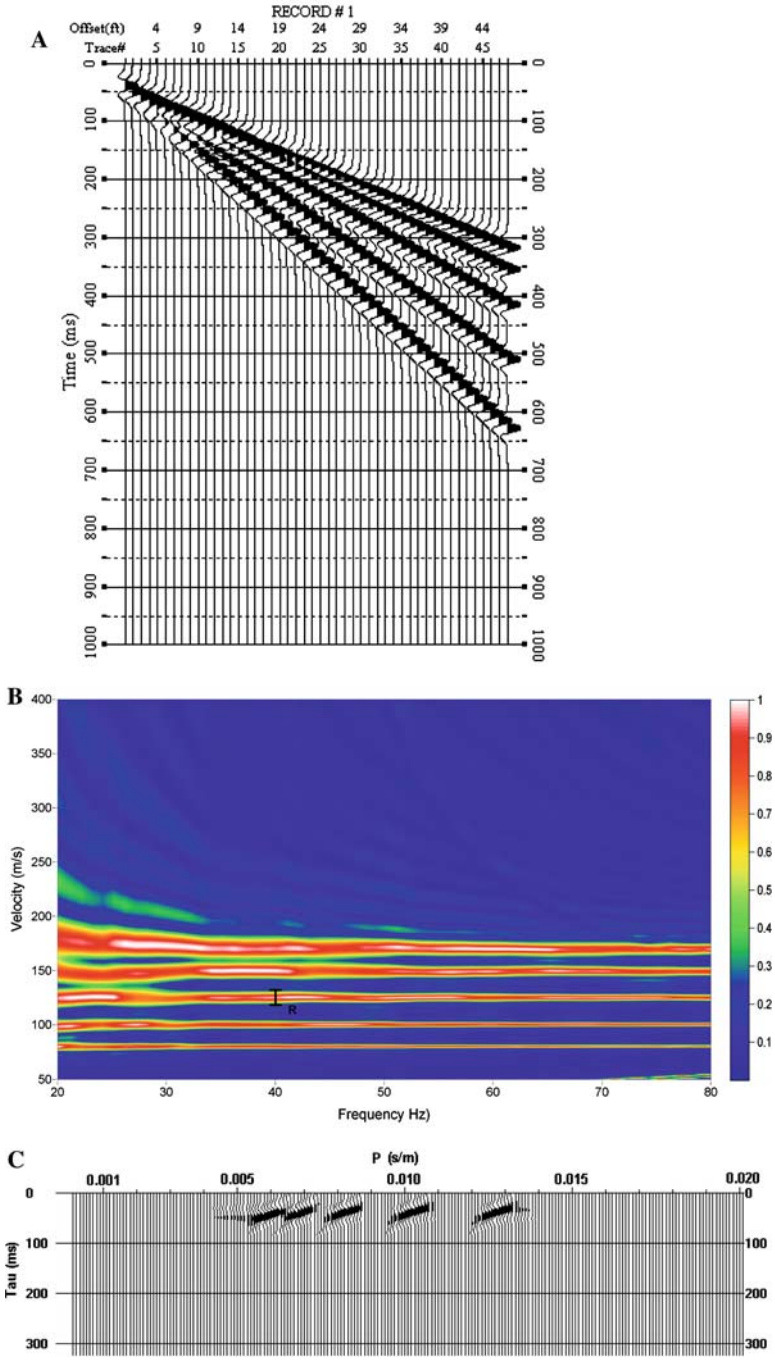
A
RECORD # 1
Offset(ft) 4 9 14 19 24 29 34 39 44
Trace# 5 10 15 20 25 30 35 40 45
Time (ms)
0 100 200 300 400 500 600 700 800 900 1000
B
Velocity (m/s)
400 350 300 250 200 150 100 50
20 30 40 50 60 70 80
Frequency Hz)
R
1 0.9 0.8 0.7 0.6 0.5 0.4 0.3 0.2 0.1
C
P (s/m)
0.001 0.005 0.010 0.015 0.020
Tau (ms)
0 100 200 300

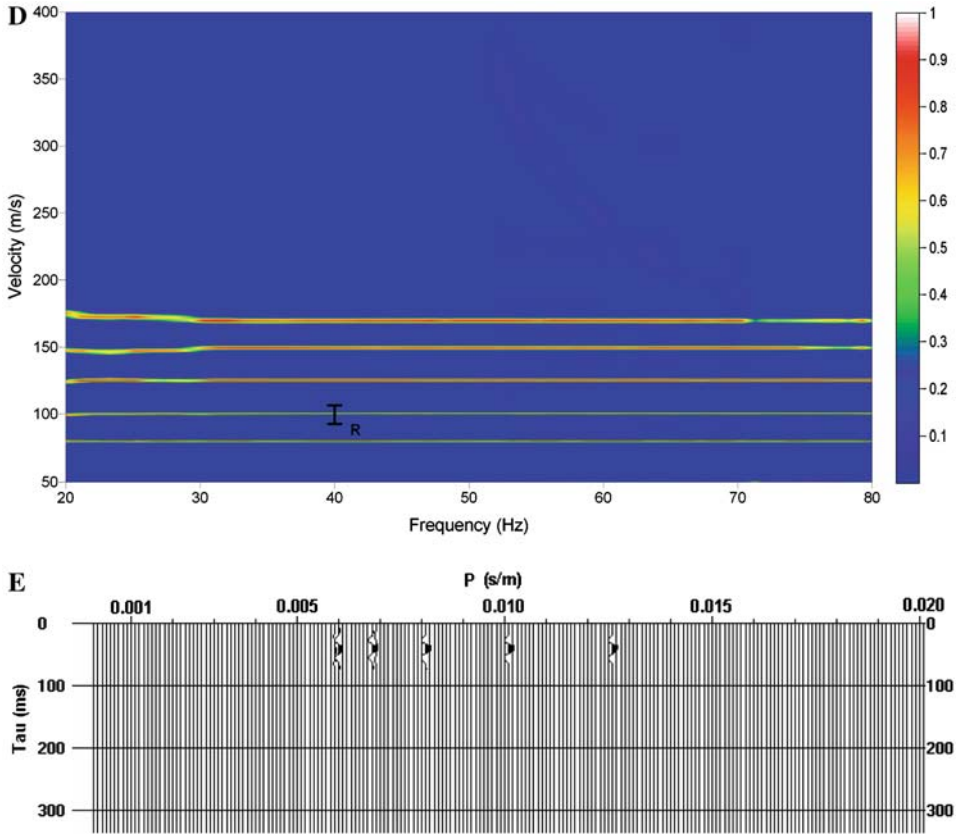

Figure 1
(a) Synthetic data containing 48 traces with five linear events. (b) Radon panel in the *f*-*v* domain and in the τ-*p* domain (c) generated by standard LRT. (d) Radon panel in the *f*-*v* domain and the in the τ-*p* domain (e) generated by high-resolution LRT.

1 m with a 1 m geophone interval. Spectrum analysis showed the data (Fig. 2a) possess a dominant frequency for Rayleigh waves of 10 Hz with a frequency band of 5 Hz to 50 Hz except for a strong DC component. The shot gather (Fig. 2a) is transformed along the time direction to the frequency domain and set the slowness p range from 0 s/m to 0.01 s/m with 0.0001 s/m interval (101 slowness points). We obtained the image in the *f*-*v* domain by high-resolution LRT using a weighted preconditioned CG algorithm (Fig. 2b).

Rayleigh-wave energy is dominant in the image (Fig. 2b). Phase velocities can be picked following higher amplitude peaks associated with energy trends. At some frequencies, for example, 22 Hz, 34 Hz, and 45 Hz, there is more than one peak due to higher modes. Asymptotes at the high and low frequencies of the fundamental mode (Fig. 2b) indicate the correct phase velocities for the top layer (~190 m/s) and the half space (~370 m/s). The image also shows strong energy for the first, second, and third

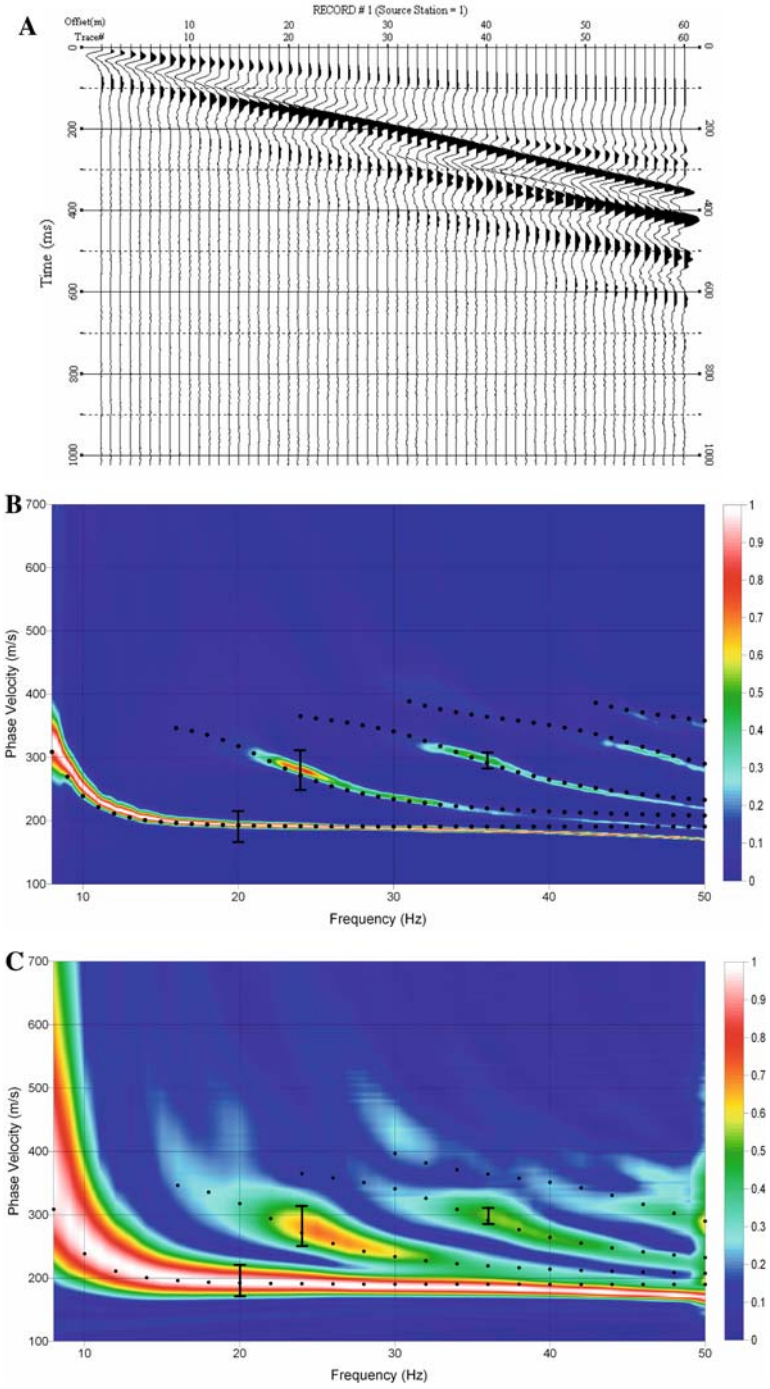
A
RECORD # 1 (Source Station = 1)
Offset(m)
Trace#
Time (ms)
B
Phase Velocity (m/s)
Frequency (Hz)
C
Phase Velocity (m/s)
Frequency (Hz)

◀ Figure 2
(a) Synthetic vertical-component data due to a two-layer model. (b) An image of dispersive energy in the *f-v* domain generated by high-resolution LRT. (c) An image of dispersive energy in the *f-v* domain generated by the slant stacking algorithm (XIA *et al*., 2007b). Solid dots were analytical results calculated by the Knopoff method (SCHWAB and KNOPOFF, 1972).

higher modes and provides sufficient resolution to distinguish these modes. Asymptotes of the higher modes also approach the correct phase velocities. Asymptotes of higher modes at the high and low frequencies reach the S-wave velocities of the top layer and the half space, respectively.

We use the analytical results (solid dots, Fig. 2b) calculated by the Knopoff method (SCHWAB and KNOPOFF, 1972) to assess the accuracy of the image. For the fundamental mode, the image indicates a relatively higher phase velocity compared with the analytical results (<5%) at frequencies around 10 Hz and a relatively lower phase velocity compared with the analytical results (<5%) in the high-frequency range (>40 Hz). For the first higher mode, the image suggests a slightly higher phase velocity compared with the analytical results (<5%) at frequencies around 25 Hz. Possible reasons include near-field effects (e.g., non-plane wave propagation and body-wave energy) and artifacts of the finite-difference approximation (XU *et al*., 2007).

As discussed in the previous section that four algorithms (e.g., YILMAZ, 1987; MCMECHAN and YEDLIN, 1981; PARK *et al*., 1998; XIA *et al*., 2007b) image the dispersive energy of surface waves with the same level of resolution, we used the slant stacking method (XIA *et al*., 2007b) to generate a dispersion image (Fig. 2c) for comparison with the high-resolution LRT results (Fig. 2b). We notice that (1) the image of dispersion energy generated by high-resolution LRT possesses much higher resolution. Lengths of double-end lines at frequencies 20, 24, and 36 Hz at different modes are the distance between half of the maximum value of dispersion energy in Figure 2c. The same double-end lines are superposed in Figure 2b. It is obvious that the double-end line almost spans one length longer than the half value in Figure 2b. We may conclude that the resolution increases more than 100% by high-resolution LRT; (2) because the image of dispersive energy in the low-frequency range possesses lower resolution is an intrinsic property (FORBRIGER, 2003), high-resolution LRT improves the resolution more than 200% in the frequency range lower than 20 Hz; and (3) dispersion energy of different modes generated by the high-resolution LRT (Fig. 2b) can more easily be distinguished, which is very important for determining phase velocities of surface waves.

4. Real-World Examples

Two real-world data were employed to study the effectiveness and applicability of high-resolution LRT for dispersive energy imaging. Surface-wave data from our first real-world example (Fig. 3a) were acquired on Virginia Key, Florida, using a 24-channel seismograph with 14-Hz vertical-component geophones that were deployed at 0.6 m

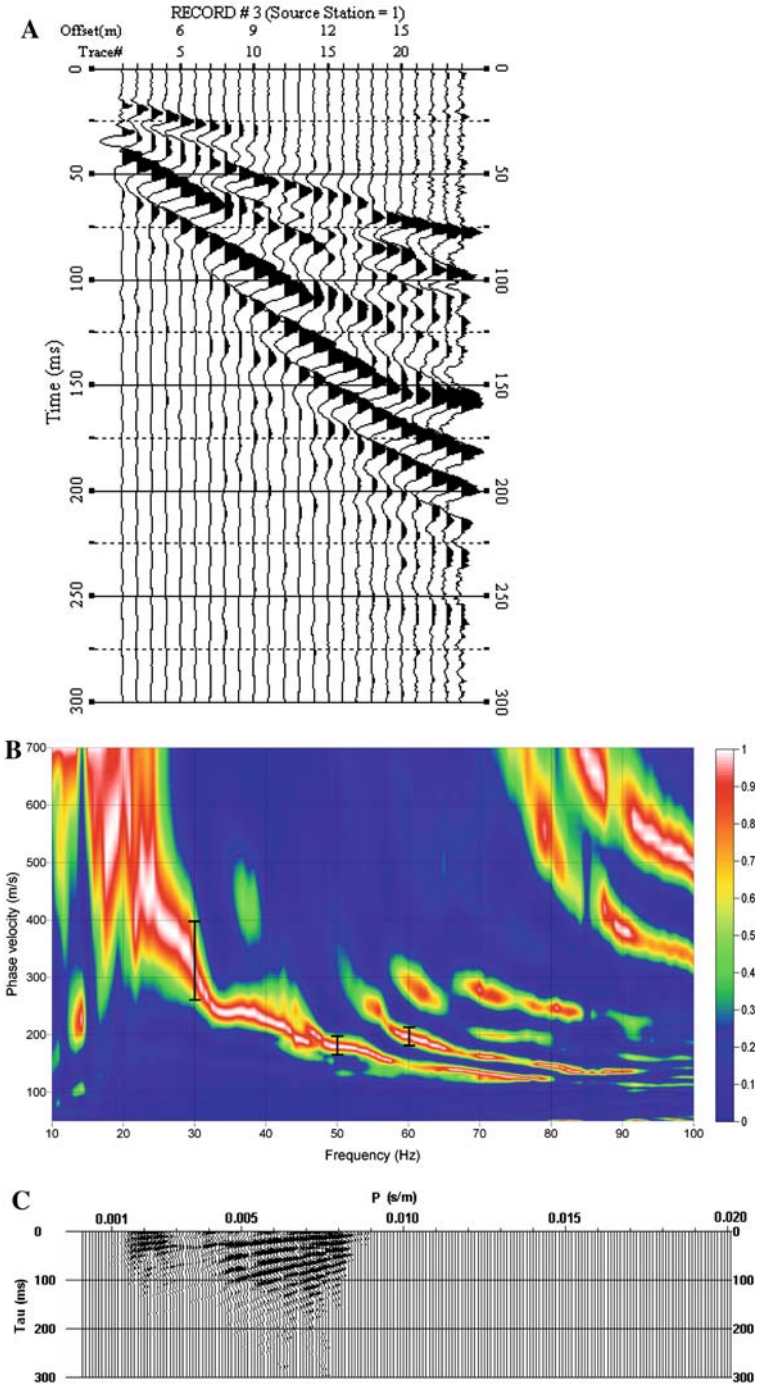
A
RECORD # 3 (Source Station = 1)
Offset(m)
Trace#
Time (ms)
B
Phase velocity (m/s)
Frequency (Hz)
C
P (s/m)
Tau (ms)

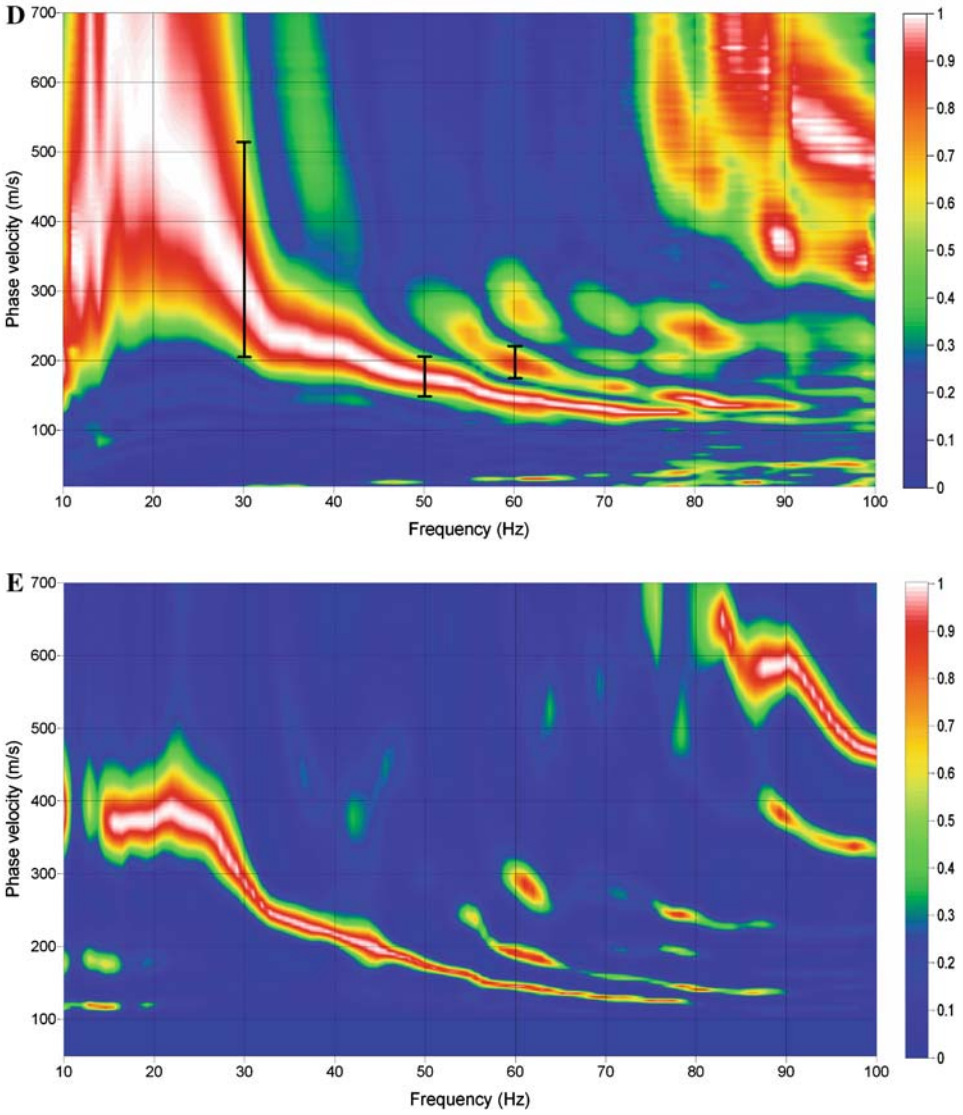

Figure 3
(a) Data acquired from Virginia Key, Florida, with a 24-channel system. (b) A dispersive image in the *f-v* domain calculated by high-resolution LRT. (c) Radon panel in the τ-*p* domain. (d) An image of dispersive energy in the *f-v* domain generated by the slant stacking algorithm (Xia *et al*., 2007b). (e) A dispersive image in the *f-v* domain calculated by high-resolution LRT using the first 21 traces.

intervals with the nearest offset of 4.5 m (Xia *et al*., 2006b 2007b) The source was a 3.5-kg hammer vertically impacting a 0.3 m by 0.3 m metal plate. Because of selections of geophones and acquisition geometry, Rayleigh-wave energy dominated the data

(Fig. 3a). The object of the survey was to use surface-wave techniques to delineate the subsurface up to 12 m depth.

Spectrum analysis showed Rayleigh waves (Fig. 3a) possess a dominant frequency around 40 Hz with a frequency band of 15 Hz to 90 Hz. The shot gather (Fig. 3a) is transformed along the time direction to the frequency domain and sets the slowness p range from 0 s/m to 0.02 s/m with 0.0001 s/m interval (201 slowness points). We obtained the image in the f-v domain by high-resolution LRT using a weighted preconditioned CG algorithm (Fig. 3b). Figure 3c shows the Radon panel in the τ-p domain, correspondingly. We can pick phase velocities by following higher amplitude peaks along energy trends (Fig. 3b). Phase velocities with the fundamental mode can be determined from 20 Hz up to 100 Hz. Phase velocities of the first higher mode can also be picked between 50 Hz and 90 Hz without difficulty.

We used the slant stacking method (XIA *et al.*, 2007b) to generate a dispersion image (Fig. 3d) for comparison with the high-resolution LRT results (Fig. 3b). We use a double-end line at frequency 30, 50, and 60 Hz at different modes between the half value of dispersion energy at Figures 3b and 3d. The lengths of the double-end line in Figure 3d are about 100%, 80%, and 40% longer than those in Figure 3b. High-resolution LRT improves the resolution of the dispersive energy, especially in a low-frequency range. The dispersion energy of higher modes generated by high-resolution LRT (Fig. 3b) possesses more distinguished trends than that generated by slant stacking (Fig. 3d), which is very helpful in picking multimodes for joint inversion (XIA *et al.*, 2003; LUO *et al.*, 2007). We also notice that the fundamental mode was not very smooth around frequency 46 Hz, which may be disturbed by body waves or noise that possess abnormally large amplitudes around 160 ms in the last three traces (traces 22 to 24). This can be demonstrated by the dispersion energy generated by high-resolution LRT using the first 21 traces (Fig. 3e). The disturbance of the fundamental mode at $\sim$46 Hz has disappeared in Fig. 3e. At the same time, the energy of the higher modes was weakened because far offset traces were dropped.

Data from our second real-world example (Fig. 4a) were acquired in Olathe, Kansas, using a 60-channel seismograph with 4.5-Hz vertical-component geophones deployed at a 0.6 m interval with the minimum offset of 6 m (MILLER *et al.*, 1999; XIA *et al.*, 2007b). The source was a 5.4-kg hammer vertically impacting a 0.3 m by 0.3 m metal plate. Dispersive energy was well developed and dominant in the recorded data (Fig. 4b). The object of the survey was to use surface-wave techniques to map a bedrock interface up to 10 m deep and to locate fracture zones to which contaminants might migrate (MILLER *et al.*, 1999). Two dead traces existed at the end of the shot gather.

Spectrum analysis showed Rayleigh waves (Fig. 4a) possess a dominant frequency around 50 Hz with a frequency band of 15 Hz to 100 Hz. The shot gather (Fig. 4a) is transformed along the time direction to the frequency domain, and the slowness p range is set from 0 s/m to 0.01 s/m with 0.0001 s/m interval (101 slowness points).

We obtained the image in the f-v domain by high-resolution LRT using a weighted preconditioned CG algorithm (Fig. 4b). Figures 4c shows the Radon panel in the τ-p

domain, correspondingly. The fundamental mode of a surface-wave energy trend was very well defined from 25 Hz to 80 Hz. We can easily pick phase velocities following higher amplitude peaks associated with the trend. Resolution of images of dispersion energy generated by high-resolution LRT (Fig. 4b) is considerably higher than those by slant stacking (Fig. 4d) although well-defined dispersive energy in both figures demonstrates the power of the slant stacking technique and high-resolution LRT in suppressing noise (two dead traces). We use a double-end line at frequencies 30 and 40 Hz of the fundamental mode between half of the maximum value of dispersion energy in Figures 4b and 4d. The lengths of the double-end line in Figure 4d are respectively about 100%, and 60% longer than those in Figure 4b. In addition, like the other four imaging algorithms, high-resolution LRT increases its ability in suppressing noise with longer receiver spread, and it effectively suppressed the last two dead traces in this example.

5. Discussion and Conclusions

We have proposed high-resolution LRT to image Rayleigh-wave dispersive energy. We first introduced the standard- and high-resolution LRT and presented synthetic data to show the process of generating the dispersive energy. Then we imaged surface-wave dispersion curves of a theoretical model and real-world examples to demonstrate the feasibility of imaging higher-resolution dispersion energy.

Rayleigh-wave dispersive energy results of the synthetic data demonstrate the following: (1) The image generated by high-resolution LRT possesses substantially higher resolution than that generated by the slant stacking algorithm (Xia *et al*., 2007b). The resolution increases more than 100%; (2) LRT improves the resolution more than 200% in the frequency range lower than 20 Hz; and (3) dispersion energy of different modes generated by the high-resolution LRT (Fig. 2c) can be very easily distinguished, which is very important in picking frequency-velocity pairs.

Rayleigh-wave dispersive energy results of real-world examples show that high-resolution LRT improves overall resolution of images of dispersive energy about 50%. Images of dispersion energy of higher modes generated by high-resolution LRT (Figs. 3b and 4b) possess more distinguished trends than those generated by slant stacking (Figs. 3d and 4d), which is very helpful in picking multi-mode data for joint inversion (Xia *et al*., 2003; Luo *et al*., 2007).

The main motivation of the present work lies in the observation that improving horizontal resolution of dispersive energy in current algorithms is a very difficult task. Modeling results (Park *et al*., 1998) show that the resolution of the dispersion image in the *f*-*v* domain will increase as the geophone spread length increases. However, doubling the geophone spread may not necessarily double resolution of the dispersion image (Xia *et al*., 2006b). At the same time, the horizontal resolution of the inverted S-wave velocity section is most influenced by the receiver-spread length and the source interval. The

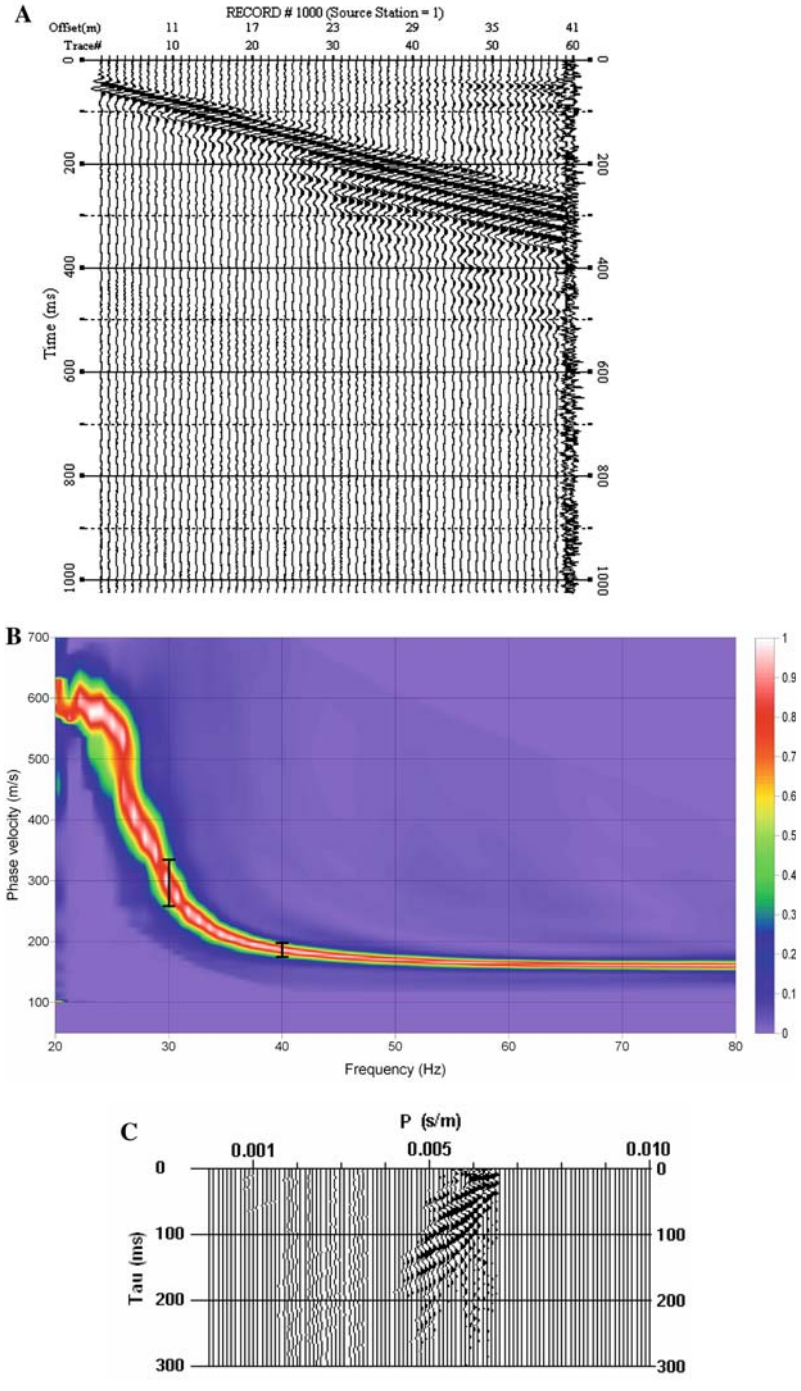
A
RECORD # 1000 (Source Station = 1)
Offset(m)
Trace#
Time (ms)
B
Phase velocity (m/s)
Frequency (Hz)
C
P (s/m)
Tau (ms)

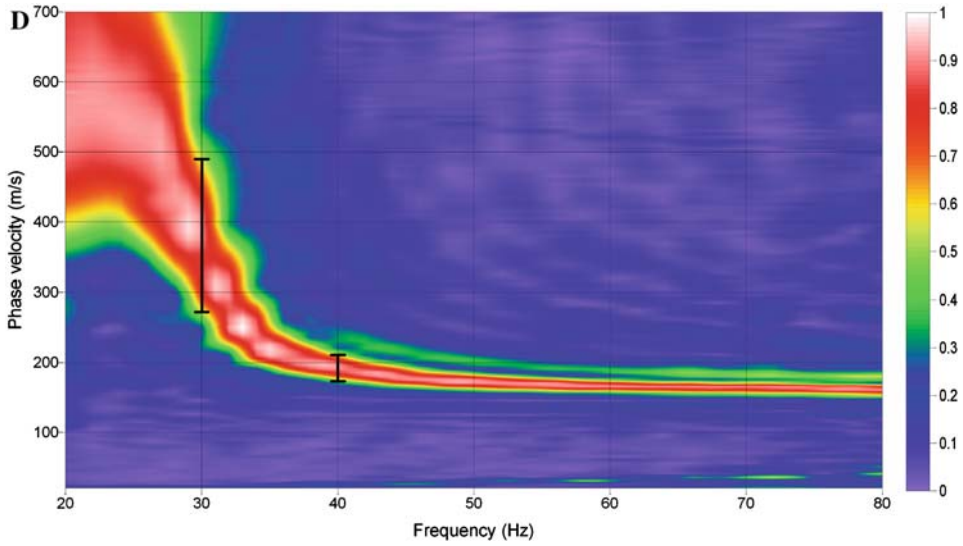

Figure 4
(a) Data acquired in Olathe, Kansas (Miller *et al*., 1999), with a 60-channel system. (b) A dispersive image in the *f-v* domain calculated by high-resolution LRT. (c) Radon panel in the τ-p domain. (d) An image of dispersive energy in the *f-v* domain generated by the slant stacking algorithm (Xia *et al*., 2007b).

receiver-spread length sets the theoretical lower limit and any *Vs* structure with its lateral dimension smaller than this length will not be properly resolved in the final *Vs* section (Xia *et al*., 2005; Luo *et al*., in review). The ultimate goal of increasing Rayleigh-wave techniques is to extract accurate dispersion curves from a record with a short geophone spread (Xia *et al*., 2005).

High-resolution LRT continues to receive considerable attention in the literature because it plays an intricate role in seismic data processing such as multiple-removal filter, data interpolation, migration, and so on (Thorson and Claerbout, 1985; Yilmaz, 1987; Foster and Mosher, 1992; Sacchi and Ulrych, 1995; Bickel, 2000; Herrmann *et al*., 2000; Trad *et al*., 2002 2003; Ethan and Matthias, 2006). We apply high-resolution LRT in imaging Rayleigh-wave dispersive energy to increase its resolution, which has been demonstrated by synthetic and real-world examples. At the same time, great effort has been spent on properly choosing key parameters, phase preservation, multimode separation algorithm, and in using high-resolution LRT, which are our current research topics.

Acknowledgments

The first author appreciates the Kansas Geological Survey, the University of Kansas, and the China Scholarship Council for the financial support to conduct this study. The

authors wish to thank Öz Yilmaz for helpful discussions and suggestions in this paper. We are particularly grateful to Mauricio D. Sacchi, Daniel Trad, and Wang Juefu for their constructive advice in high-resolution LRT programming. The authors thank Brahim Abbad and Brian Mitchell for their constructive and detailed reviews. The authors thank Marla Adkins-Heljeson of the Kansas Geological Survey for editing the manuscript.

References

Bickel, S.H. (2000), *Focusing aspects of the hyperbolic Radon transform*, Geophys. *65*, 652–655.

Calderón-Macías, C. and Luke, B. (2007), *Improved parameterization to invert Rayleigh-wave data for shallow profiles containing stiff inclusions*, Geophys. *72*(1), U1–U10.

Claerbout, J.F. *Earth Sounding Analysis: Processing versus Inversion* (Blackwell Scientific Publications, Inc. (1992)).

Coruh (1985).

Dal Moro, G., Pipan, M., Forte, E. and Finetti, I. (2003), *Determination of Rayleigh-wave dispersion curves for near surface applications in unconsolidated sediments*, Tech. Program with Biographies, SEG, 73rd Annual Meeting, Dallas, TX. 1247–1250.

Dal Moro, G. and Pipan, M. (2007), *Joint inversion of surface wave dispersion curves and reflection travel times via multi-objective evolutionary algorithms*, J. Appl. Geophys. *61*(1), 56–81.

Dunne, J. and Beresford, G. (1995), *A review of the τ-p transform, its implementation and its applications in seismic processing*, Exploration Geophys. *26*, 19–36.

Ethan, J.N. and Matthias, G.I. (2006), *Amplitude preservation of Radon-based multiple-removal filters*, Geophys. *71*(5), V123–V126.

Forbriger, T. (2003), *Inversion of shallow-seismic wavefields: I. Wavefield transformation*, Geophys. J. Internat. *153*, 719–734.

Foster, D.J. and Mosher, C.C. (1992), *Suppression of multiple reflections using the Radon transform*, Geophys. *57*, 386–395.

Herrmann, P., Mojesky, T. and Hugonnet, P. (2000), *Dealiased high-resolution Radon transforms*, 70th Ann. Internat. Meeting, SEG, Expanded Abstracts. 1953–1956.

Ivanov, J., Miller, R.D., Xia, J., Steeples, D.W. and Park, C.B. (2006a), *Joint analysis of refractions with surface waves: An inverse solution to the refraction-travel time problem*, Geophys. *71*(6), R131–R138.

Ivanov, J., Miller, R.D., Lacombe, P., Johnson, C.D. and Lane, J.W., Jr. (2006b), *Delineating a shallow fault zone and dipping bedrock strata using multichannel analysis of surface waves with a land streamer*, Geophys. *71*, A39–A42.

Ji, J. (2006), *CGG method for robust inversion and its application to velocity-stack inversion*, Geophys. *71*(4), R59–R67.

Lai, C.G., Rix, G. J., Foti, S. and Roma, V. (2002), *Simultaneous measurement and inversion of surface wave dispersion and attenuation curves*, Soil Dyn. Earthq. Eng. *22*, 923–930.

Luigia, N. and Tatiana, Q. (2004), *Improvement in GPR coherent noise attenuation using τ-p and wavelet transforms*, Geophys. *69*(3), 789–802.

Luo, Y., Xia, J., Liu, J., Xu, Y. and Liu, Q. (in press), *Generation of a pseudo-2D shear-wave velocity section by inversion of a series of 1D dispersion curves*, J. Appl. Geophys, in press.

Luo, Y., Xia, J., Liu, J., Liu, Q., and Xu, S. (2007), *Joint inversion of high-frequency surface waves with fundamental and higher modes*, J. Appl. Geophys. *62*, 375–384.

Maeland, E. (2004), *Sampling, aliasing, and inverting the linear Radon transform*, Geophys. *69*(3), 859–861.

Marfurt, K.J. and Schneider, R.V. (1996), *Pitfalls of using conventional and discrete Radon transforms on poorly sampled data*, Geophys. *61*(5), 1467–1482.

Mayne, W.H. (1962), *Horizontal data stacking techniques*, Supplement to Geophysics *27*, 927–937.

McMechan, G.A. and Yedlin, M.J. (1981), *Analysis of dispersive waves by wavefield transformation*, Geophys. *46*, 869–874.

MENKE, W., *Geophysical Data Analysis: Discrete Inverse Theory* (Academic Press, Inc., Orlando, FL (1984)).

MILLER, R.D., XIA, J., PARK, C.B., and IVANOV, J. (1999), *Multichannel analysis of surface waves to map bedrock*, The Leading Edge *18*, 1392–1396.

PARK, C.B., MILLER, R.D. and XIA, J. (1998), *Imaging dispersion curves of surface waves on multi-channel record*, Technical Program with Biographies SEG, 68th Annual Meeting, New Orleans, LA., 1377–1380.

PARK, C.B., MILLER, R.D. and XIA, J. (1999), *Multi-channel analysis of surface waves* (MASW), Geophys. *64*, 800–808.

SACCHI, M. and ULRYCH, T. (1995), *High resolution velocity gathers and offset space reconstruction*, Geophys. *60*, 1169–1177.

SACCHI, M. and PORSANI, M. (1999), *Fast high resolution parabolic RT*, 69th Ann. Internat. Meeting, Soc. Exploration Geophysicists, Expanded Abstracts. 1477–1480.

SCHONEWILLE, M.A. and DUIJNDAM, A.J.W. (2001), *Parabolic Radon transform, sampling and efficiency*, Geophys. *66*(2), 667–678.

SCHWAB, F.A. and KNOPOFF, L., *Fast surface wave and free mode computations, in Methods in Computational Physics*, ed. B.A. Bolt: pp. 87–180 (Academic Press, New York (1972).

SONG, Y.Y., CASTAGNA, J.P., BLACK, R.A. and KNAPP, R.W. (1989), *Sensitivity of near-surface shear-wave velocity determination from Rayleigh and Love waves*, Technical Program with Biographies, SEG, 59th Annual Meeting, Dallas, TX, 509–512.

TARANTOLA, A., *Inverse Problem Theory* (Elsevier Science Publishing (1987)).

THORSON, J. R. and CLAERBOUT, J. F. (1985), *Velocity stack and slant stochastic inversion*, Geophys. *50*, 2727–2741.

TIAN, G., STEEPLES, D.W., XIA, J. and SPIKES, K.T. (2003a), *Useful resorting in surface wave method with the autojuggie*, Geophys. *68*(6), 1906–1908.

TIAN, G., STEEPLES, D.W., XIA, J., MILLER, R.D., SPIKES, K.T. and RALSTON, M.D. (2003b), *Multichannel analysis of surface wave method with the autojuggie*, Soil Dyn. Earthq. Engin. *23*(3), 243–247.

TRAD, D., ULRYCH, T. and SACCHI, M. (2002), *Accurate interpolation with high-resolution time-variant Radon transforms*, Geophys. *67*(2), 644–656.

TRAD, D., ULRYCH, T. and SACCHI, M. (2003), *Latest views of the sparse Radon transform*, Geophys. *68*, 386–399.

TURNER, G. (1990), *Aliasing in the tau-p transform and the removal of spatially aliased coherent noise*, Geophys. *55*, 1496–1503.

WANG, Y.H. (2003), *Multiple attenuation: coping with the spatial truncation effect in the Radon transform domain*, Geophys. Prospect. *51*, 75–87.

WILSON, C. and GUITTON, A. (2007), *Teleseismic wavefield interpolation and signal extraction using high-resolution linear Radon transforms*, Geophys. J. Internat. *168*, 171–181.

XIA, J., MILLER, R.D. and PARK, C.B. (1998), *Construction of vertical section of near-surface shear-wave velocity from ground roll*, Technical Program, Soc. Exploration Geophysicists and Chinese Petroleum Society Beijing 98' International Conf. pp 29–33.

XIA, J., MILLER, R.D., and PARK, C.B. (1999), *Estimation of near-surface shear-wave velocity by inversion of Rayleigh wave*, Geophys. *64*, 691–700.

XIA, J., MILLER, R.D., PARK, C.B., HUNTER, J.A., HARRIS, J.B. and IVANOV, J. (2002a), *Comparing shear-wave velocity profiles from multichannel analysis of surface wave with borehole measurements*, Soil Dyn. Earthq. Engin. *22*(3), 181–190.

XIA, J., MILLER, R.D., PARK, C.B., WIGHTMAN, E., and NIGBOR, R. (2002b), *A pitfall in shallow shear-wave refraction surveying*, J. Appl. Geophys. *51*(1), 1–9.

XIA, J., MILLER, R.D., PARK, C.B., and TIAN, G. (2002c), *Determining Q of near-surface materials from Rayleigh waves*, J. Appl. Geophys. *51*(2–4), 121–129.

XIA, J., MILLER, R.D., PARK, C.B., and TIAN, G. (2003), *Inversion of high frequency surface waves with fundamental and higher modes*, J. Appl. Geophy. *52*(1), 45–57.

XIA, J., CHEN, C., LI, P.H., and LEWIS, M.J. (2004), *Delineation of a collapse feature in a noisy environment using a multichannel surface wave technique*, Geotechnique *54*(1), 17–27.

XIA, J., CHEN, C., TIAN, G., MILLER, R.D., and IVANOV, J. (2005), *Resolution of high-frequency Rayleigh-wave data*, J. Environm. Engin. Geophys. *10*(2), 99–110.

XIA, J., XU, Y., MILLER, R.D., and CHEN, C. (2006a), *Estimation of elastic moduli in a compressible Gibson half-space by inverting Rayleigh wave phase velocity*, Surveys in Geophys. *27*(1), 1–17.

XIA, J., XU, Y., CHEN, C., KAUFMANN, R.D., and LUO, Y. (2006b), *Simple equations guide high-frequency surface-wave investigation techniques*, Soil Dyn. Earthq. Engin. *26*(5), 395–403.

XIA, J., NYQUIST, J.E., XU, Y., ROTH, M.J.S., and MILLER, R.D. (2007a), *Feasibility of detecting near-surface feature with Rayleigh-wave diffraction*, J. Appl. Geophys. *62*(3), 244–253.

XIA, J., XU, Y., and MILLER, R.D. (2007b), *Generating image of dispersive energy by frequency decomposition and slant stacking*, Pure. Appl. Geophys. *164*(5), 941–956.

XU, Y., XIA, J. and MILLER, R.D. (2007), *Numerical investigation of implementation of air-earth boundary by acoustic-elastic boundary approach*, Geophys. *72*, SM147–SM153.

YILMAZ, Ö. (1987), *Seismic data processing*, Soc. Exploration Geophysicists, Tulsa, OK.

YILMAZ, O. and TANER, M.T. (1994), *Discrete plane-wave decomposition by least-mean- square-error method*, Geophys. *59*(6), 973–982.

YILMAZ, Ö. and ESER, M. (2002), *A unified workflow for engineering seismology,* Technical Program with Biographies, SEG, 72nd Annual Meeting, Salt Lake City, UT, 1496–1499.

ZHOU, B. and GREENHALGH, S. A. (1994), *Linear and parabolic τ-p transforms revisited*, Geophys. *59*, 1133–1149.

(Received November 21, 2007, revised February 12, 2008, accepted February 12, 2008)
Published Online First: May 10, 2008